AUTHOR QUERY FORM

ELSEVIER	**Journal:** EPSL	**Please e-mail your responses and any corrections to:**
	Article Number: 118231	**E-mail:** corrections.esch@elsevier.vtex.lt

Dear Author,

Please check your proof carefully and mark all corrections at the appropriate place in the proof. **It is crucial that you NOT make direct edits to the PDF using the editing tools as doing so could lead us to overlook your desired changes.** Rather, please request corrections by using the tools in the Comment pane to annotate the PDF and call out the changes you would like to see. To ensure fast publication of your paper please return your corrections within 48 hours.

For correction or revision of any artwork, please consult *http://www.elsevier.com/artworkinstructions*

Any queries or remarks that have arisen during the processing of your manuscript are listed below and highlighted by flags in the proof.

Location in article	Query / Remark: Click on the Q link to find the query's location in text Please insert your reply or correction at the corresponding line in the proof
Q1	Your article is registered as a regular item and is being processed for inclusion in a regular issue of the journal. If this is NOT correct and your article belongs to a Special Issue/Collection please contact <j.ramkumar@elsevier.com> immediately prior to returning your corrections. (p. 1/ line 1)
Q2	The author names have been tagged as given names and surnames (surnames are highlighted in teal color). Please confirm if they have been identified correctly and are presented in the desired order. (p. 1/ line 16)
Q3	Please indicate which author(s) should be marked as 'Corresponding author'. (p. 1/ line 17)
Q4	Please check the e-mail address that has been added for author S. Racano, and correct if necessary. (p. 1/ line 63)
Q5	The Data Availability information was present in the original manuscript and also supplied in the additional file. Only the information from the original manuscript has been used (it contains more details), please check if correct. (The information in the additional file is more concise.) (p. 12/ line 112)
Q6	IMPORTANT!!! Please note that your MS Word manuscript was converted to LaTeX in the appropriate Journal layout and style. Therefore, the final proof might have some flaws. Kindly please check your proof carefully in this regard. (p. 1/ line 53)
Q7, Q8, Q9, Q10, Q11, Q12, Q13, Q14, Q15, Q16	Note that some references in the text were modified (the year or author names changed) to conform to the entries in the Reference list. Please check and amend if necessary. (p. 1/ line 59; p. 2/ line 17,20,35,106,117,128; p. 4/ line 28,29,34)
Q17	In the references list "Yildirim et al. (2013a) and (2013b)" are mentioned as separate references. Therefore citation of "Yildirim et al. (2013)" has been changed to "Yildirim et al. (2013a, 2013b)". Please amend the citation in the text if necessary. (p. 10/ line 60)
Q18	Please check if sponsor name has been identified correctly and correct if necessary. (p. 16/ line 5)
Q19, Q20	Please provide the grant numbers for the sponsors: "MIUR" and "PRIN 2017-2020 funding scheme". (p. 12/ line 128,130)

Thank you for your assistance.

Location in article	Query / Remark: Click on the Q link to find the query's location in text Please insert your reply or correction at the corresponding line in the proof
	Please check this box or indicate your approval if you have no corrections to make to the PDF file ☐

Contents lists available at ScienceDirect

Earth and Planetary Science Letters

journal homepage: www.elsevier.com/locate/epsl

Rock-uplift history of the Central Pontides from river-profile inversions and implications for development of the North Anatolian Fault

Simone Racano[a,b], Taylor Schildgen[b,a], Paolo Ballato[c], Cengiz Yıldırım[d,a], Hella Wittmann[b]

[a] University of Potsdam, Department of Geosciences, Potsdam, Germany
[b] GFZ German Research Centre for Geosciences, Potsdam, Germany
[c] University of Roma Tre, Department of Science, Rome, Italy
[d] Eurasia Institute of Earth Sciences, Istanbul Technical University, Istanbul, Turkey

A R T I C L E I N F O

Article history:
Received 30 August 2022
Received in revised form 28 April 2023
Accepted 17 May 2023
Available online xxxx
Editor: J.-P. Avouac

Dataset link: https://doi.org/10.5281/zenodo.7577077

Keywords:
North Anatolian Fault
Central Pontides
^{10}Be denudation rates
river-profile inversion

A B S T R A C T

Major strike-slip fault systems on Earth, like the North Anatolian Fault (NAF), play an important role in accommodating plate motion, but surprisingly little is known about how such structures evolve through space and time. Along the central sector of the NAF in the Central Pontides, transpression and crustal thickening along the northward restraining bend of the fault are thought to have generated rock-uplift rates of 0.2–0.3 km/Myr since at least 400 ka based on Quaternary marine and river terraces, while data from low-temperature thermochronology suggest that an enhanced exhumation phase occurred within the last 11 Myr. However, the precise onset of this faster uplift phase, which likely reflects deformation associated with the development of the central sector of the NAF, is poorly constrained.

Here we define the spatiotemporal pattern of rock-uplift rates within the Central Pontides over the last ∼ 10 Myr by performing linear inversions of 19 river profiles that drain the northern margin of the Central Pontides, from the Sinop Range to the Black Sea. We use 21 new ^{10}Be-derived basin-average denudation rates to calibrate an erodibility parameter, which we use to convert our χ-transformed river profiles into rock-uplift histories. Our results document an increase in rock-uplift rates after 10 Ma, with peak rates of ∼0.15–0.25 km/Myr occurring between 4 and 2 Ma. Moreover, the spatiotemporal pattern of uplift suggests that faster rock uplift started in the eastern part of the Sinop Range and migrated westward over a period of ca. 2 to 2.5 Myr, which we relate to the westward propagation of the NAF through this sector at a rate of 74 ± 13 km/Myr. In the context of previously published constraints on the westward propagation of the NAF starting in eastern Turkey at ∼12 Ma, our results suggest differences in fault-propagation rates that coincide with differences in the orientation of the NAF relative to plate-convergence velocity vectors. Fault segments with higher obliquity appear to have propagated at rates up to 2-fold slower than those oriented more parallel to the plate-convergence vector.

1. Introduction

The North Anatolian Fault (NAF) is one of the world's longest and most active strike-slip faults, stretching over a distance of ca. 1600 km and currently accommodating ca. 24 mm/yr of dextral motion between the Anatolian and Eurasian plates (Barka and Hancock, 1984; Hubert-Ferrari et al., 2002; Şengör et al., 2005; Le Pichon et al., 2016) (Fig. 1a). Despite the major role of the NAF in accommodating plate motion, only a few studies have contributed to understanding how and when this structure evolved. Those studies have mostly relied on lithostratigraphic correlations of deformed sediments within basins along the NAF together with sparse biostratigraphic age constraints (e.g., Barka and Hancock, 1984; Hubert-Ferrari et al., 2002; Şengör et al., 1985, 2005), studies of deformed offshore sediments (e.g., Karakaş et al., 2018), or offset geologic/geomorphic markers (e.g., Yıldırım and Tüysüz, 2017). Current estimates are that the NAF first formed in eastern Anatolia between 13 and 11 Ma (Şengör et al., 2005, and references within), propagated westward into central Anatolia between

E-mail address: racano@uni-potsdam.de (S. Racano).

https://doi.org/10.1016/j.epsl.2023.118231
0012-821X/© 2023 Elsevier B.V. All rights reserved.

the late Miocene and early Pliocene (Barka and Hancock, 1984; Hubert-Ferrari et al., 2002; Şengör et al., 2005), and reached the Marmara Sea either in the latest Miocene/early Pliocene (Karakaş et al., 2018) or in the Pleistocene (Şengör et al., 2005; Sorlien et al., 2012). Apart from considering this general east-to-west propagation of strain localization to form the NAF (Şengör et al., 2005), no studies have considered the details of how and why fault propagation rates may have varied along the 1600-km fault trace.

Constraints on the development of the NAF along its central sectors are particularly poor. Central Anatolia marks a transitional tectonic regime between extension in the western Aegean and compression in eastern Anatolia. Although sedimentary basins of Central Anatolia show evidence for extension starting in the middle (Koç et al., 2012) to late Miocene (Koçyiğit et al., 2001) or early Pliocene (Krystopowicz et al., 2020), the Central Pontides, which lie north of the broad restraining bend of the NAF, have experienced shortening over a similar timeframe (Yildirim et al., 2011; Espurt et al., 2014; Ballato et al., 2018). Considering that this shortening has been linked to transpressional deformation associated with the broad restraining bend of the NAF (Yildirim et al., 2011), the rock-uplift history of the Central Pontides provides an alternative path to dating the development of the central sector of the NAF.

A few studies have estimated the onset of enhanced rock uplift or surface uplift in the Central Pontides. Stable isotope studies from sedimentary basins in Central Anatolia reveal that the Central Pontides grew sufficiently tall to form an orographic barrier to precipitation sometime after 8 Ma (Mazzini et al., 2013). Apatite (U-Th)/He ages from the Sinop Range (Fig. 1c) show that the western portion of the range experienced increased rock uplift and exhumation sometime after 11 Ma, but late Cenozoic exhumation farther east is too limited to be resolved by this method (Ballato et al., 2018). The high-elevation (1 to 1.5 km), low-relief surfaces that cap some high-elevation portions of the Central Pontides also indicate increased rock-uplift rates sometime after the development of those surfaces (Yildirim et al., 2011), but it is unknown when they formed. Other studies of the rock-uplift or river-incision history are limited to Quaternary timescales. Nevertheless, extrapolation of river incision rates within the Central Pontides of 0.3 to 0.45 mm/yr (averaged over the last several hundreds of kyr; Yildirim et al., 2013a) or marine-terrace derived rock-uplift rates of 0.15 to 0.3 mm/yr averaged over the last several hundreds of kyr (Yildirim et al., 2013b; Berndt et al., 2018) to the 1 to 1.5 km elevation of the low-relief surfaces implies that the faster rock-uplift phase could have started between ~3 and 10 Ma.

To improve these constraints on the rock-uplift history of the Central Pontides, and provide quantitative new constraints on the development of the central portion of the NAF, we invert river longitudinal profiles for rock-uplift histories (e.g., Goren et al., 2014; Gallen, 2018). This approach assumes block uplift (i.e., spatially uniform uplift) of a river catchment, with variations in rock-uplift rates through time reflected by variations in channel steepness, propagating upstream at a predictable rate. Considering that the river steepness is determined not only by the rock-uplift rate it has experienced, but also by the erodibility of the bedrock, we use 21 new in-situ ^{10}Be-derived catchment average denudation rates to calibrate an erodibility parameter. Moreover, we explore the influence of variable lithologies that outcrop in the field area on that erodibility parameter. Similar to a study recently performed in the Central Taurides of south-central Anatolia (Fig. 1b, Racano et al., 2021), we use river-profile inversions from river catchments spanning the length of the mountain range and perpendicular to the main structures to determine the spatio-temporal pattern of rock uplift. Because several channel profiles within the Central Pontides show a transient form that reflects a change in rock-uplift rates through time, this approach allows us to bridge the timescale gap associated with the previous thermochronologic and geomorphic constraints, and more tightly identify the onset of faster rock uplift. With our new data to constrain the development of the NAF in central Turkey, together with updated constraints from the literature and other data on deformation patterns, we propose a refined model for the evolution of this major fault between eastern Turkey and the Marmara Sea over the last ~12 Myr.

2. Geological background

The ~E-W-oriented Pontide mountains stretch along the northern coast of Turkey between the Black Sea and the Tauride-Anatolide and Kırşehir microcontinents (Fig. 1; Okay and Topuz, 2017 and references therein). The range has been built over the former southern margin of the Eurasian Plate through multiple events of oceanic subduction, continental collision, magmatic accretion and back-arc extension (see Supplementary Material for details on the origin of different rocks exposed in the Central Pontides and their composition).

The Sinop Range represents a large-scale, south-verging anticline (Sinop Anticline) dissected by minor reverse faults (Fig. 1d; Espurt et al., 2014; Ballato et al., 2018). Thermal modeling from granitoids exposed in the core of the range (where exhumation is greatest), combined with stratigraphic information and available seismic lines, document an initial episode of thrusting and exhumation from ~40 to 20 Ma (Espurt et al., 2014; Ballato et al., 2018). Deformation occurred along the north-dipping Ekinveren Fault (Fig. 1c-d), a tectonic boundary that first controlled the locus of the basin depocenters during the late Cretaceous rifting and later accommodated the Eocene-Oligocene tectonic inversion (Ballato et al., 2018).

After a phase of limited tectonic activity and erosion that led to the formation of a low-relief landscape (Fig. 1c), the Ekinveren Fault was reactivated as thrust fault sometime after 11 Ma (Ballato et al., 2018), leading to the uplift of the Sinop Range. The amount of exhumation increases toward the western boundary of the fault, where exhumational cooling since 11 Ma is about 60 °C (Ballato et al., 2018). The onset of faulting and the asymmetric distribution of fault-related exhumation appears to have been controlled by the inception of the North Anatolian Fault and its northward-convex geometry (Yildirim et al., 2011). Toward the east, the activity of the Ekinveren Fault decreases gradually, and the Sinop Range becomes sub-parallel to the North Anatolian Fault, whereas to the west, the arc-shaped geometry of the Central Pontides is completed by the NE-SW trending Karabük Range (Fig. 1c). This range is bounded by the NW-dipping Karabük thrust fault and a few minor SE-dipping thrust faults. Finally, a conjugate system of south-dipping thrust faults cutting the northern limb of the Sinop Anticline occurs along the eastern (Balıfakı and Erikli faults) and the westernmost sectors of the range (Cide Fault) (Fig. 1c-d), whereas in the center, this system likely continues offshore, as suggested by earthquake focal mechanisms (Yildirim et al., 2011).

3. Methods

3.1. Catchment-average denudation rates from ^{10}Be in detrital sands

We collected river sands from 21 locations in 2015, which were selected to span a wide range of average channel steepness (k_s) values in the upstream contributing catchments. Samples were processed at the GeoForschungsZentrum (GFZ) Potsdam HELGES laboratory following standard procedures (von Blanckenburg et al., 2004; Wittmann and von Blanckenburg, 2016). Quartz from the 250-710 μm size fraction was concentrated through magnetic separation followed by HCl and H_2O_2 treatment to dissolve carbonates and organic material, then leached in a 2%HF/2%HNO_3 solution at least three times for 12 h each in an ultrasonic bath to dissolve

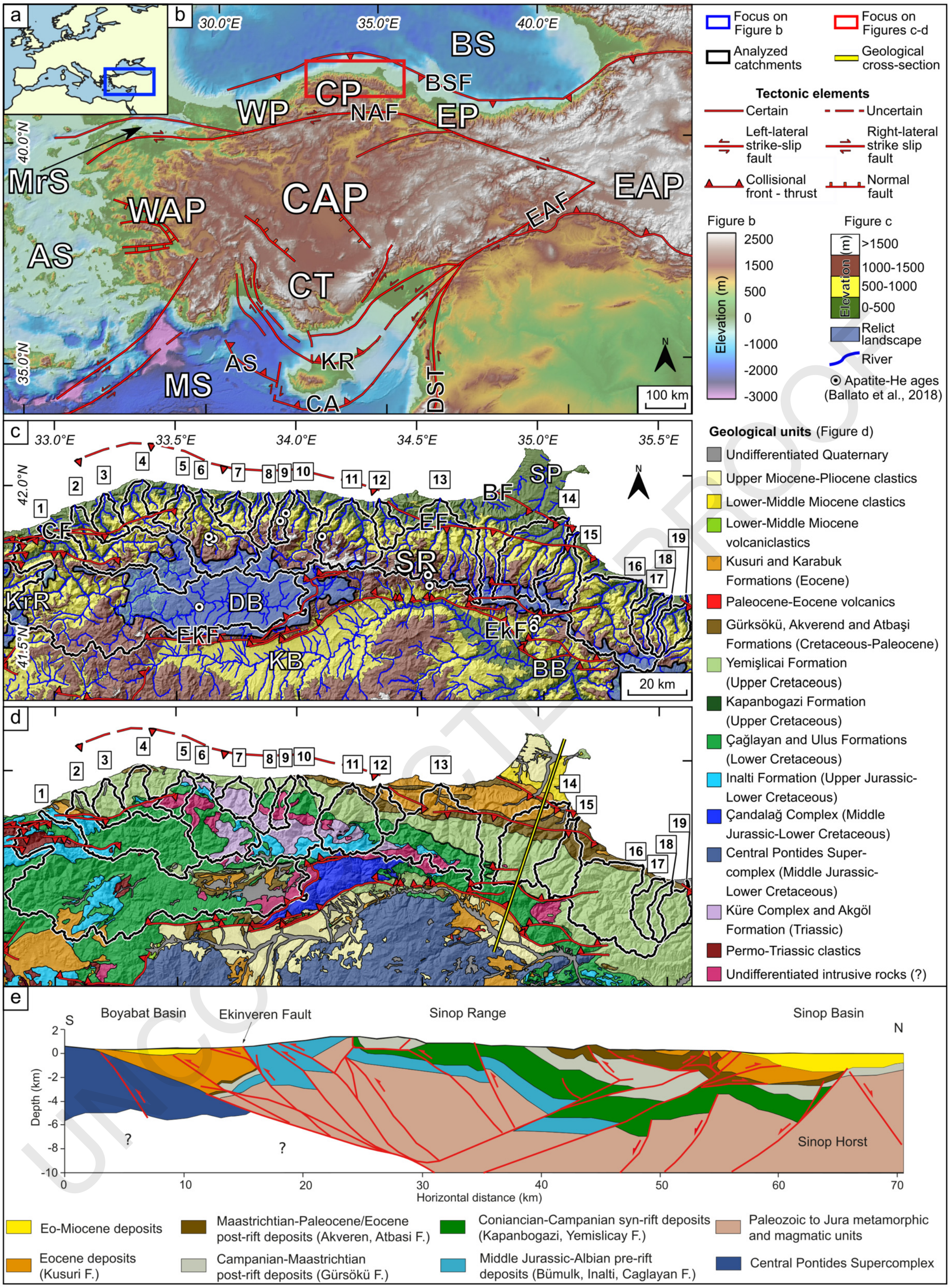

Fig. 1. Geological and morphological settings of the Central Pontides. (a) Location of the Anatolian plate (blue box). (b) Regional tectonic boundaries and topography of the Anatolian plate (modified from Racano et al., 2021); white labels indicate the main tectonic regions, black labels the main tectonic structures. CAP: Central Anatolian Plateau; EAP: Eastern Anatolian Plateau; WAP: Western Anatolian Province; WP: Western Pontides; CP: Central Pontides; EP: Eastern Pontides; CT: Central Taurides; NAF: North Anatolian Fault; BSF: Black Sea Fault; EAF: East Anatolian Fault; DST: Death Sea Transform Fault; CA: Cyprus Arc; PT: Paphos Transform; AS: Antalya Slab; BS: Black Sea; MrS: Marmara Sea; AS: Aegean Sea; MS: Mediterranean Sea. The red box shows the Sinop Range. (c) Map of the Sinop Range showing elevations, the most relevant topographic features (white labels), drainage system, main tectonic structures (black labels) and catchments for which river-profile inversions were performed (boxed numbers). SR: Sinop Range; SP: Sinop Peninsula; KrR: Karabük Range; DB: Devrekani Basin; KB: Kastamonu Basin; BB: Boyabat Basin; BF: Balıfakı Fault; EF: Erikli Fault; CF: Cide Fault; EkF: Ekinveren Fault. (d) Geological map of the Sinop Range redrawn after Şenel (2002), and trace of the geological cross-section. (e) Geological cross-section (modified from Ballato et al., 2018).

Table 1
^{10}Be sample location, results, and calculated denudation rates.

Sample name	Latitude[a] (°N)	Longitude[a] (°E)	Elevation[a] (m)	Qtz dissolved (g)	^{9}Be carrier added (mg)	$^{10}Be/^{9}Be$ measured[b] $\times 10^{-13}$	^{10}Be conc.[c] (10^4 atoms g^{-1})	Denudation rate[d,e] (mm yr^{-1})
KHY	41.12036	32.53840	415	20.89	0.17056	0.417 ± 0.025	2.121 ± 0.056	0.302 ± 0.0189
HSR	41.10784	32.27251	396	20.90	0.17009	0.486 ± 0.028	2.488 ± 0.056	0.224 ± 0.0140
SNE	41.34238	32.80792	780	20.95	0.17032	11.330 ± 0.365	61.412 ± 0.056	0.009 ± 0.0006
KNK	41.44022	32.33950	106	21.60	0.17071	0.907 ± 0.054	4.641 ± 0.054	0.095 ± 0.0061
CYY	41.92809	33.20277	68	19.16	0.17002	0.676 ± 0.034	3.843 ± 0.061	0.113 ± 0.0072
KUR	41.84743	33.65518	488	20.78	0.17009	1.163 ± 0.051	6.207 ± 0.056	0.099 ± 0.0062
KLG	41.80527	33.75338	971	20.94	0.17002	3.717 ± 0.130	20.008 ± 0.056	0.036 ± 0.0023
YKR	41.96829	33.97049	23	20.90	0.17017	1.683 ± 0.066	9.004 ± 0.056	0.069 ± 0.0043
KRO	41.75798	34.23026	1486	22.36	0.16979	6.611 ± 0.219	33.395 ± 0.052	0.029 ± 0.0018
CDG	41.83584	34.26541	261	21.22	0.16955	0.948 ± 0.043	4.912 ± 0.055	0.136 ± 0.0085
CKY	41.84967	34.58852	207	21.92	0.16979	0.845 ± 0.050	4.227 ± 0.053	0.143 ± 0.0090
TKR	41.82071	34.77125	476	20.78	0.17094	1.477 ± 0.061	7.961 ± 0.056	0.076 ± 0.0048
YDB	41.79774	35.02775	245	21.92	0.17009	0.704 ± 0.035	3.504 ± 0.053	0.158 ± 0.0100
RCL	41.57830	35.18642	455	20.27	0.17048	1.945 ± 0.076	10.772 ± 0.058	0.059 ± 0.0037
EKR	41.58211	34.79447	514	21.63	0.17017	0.995 ± 0.046	5.083 ± 0.054	0.124 ± 0.0078
BZL	41.47409	34.64169	575	9.21	0.16994	0.892 ± 0.044	10.646 ± 0.127	0.054 ± 0.0034
UNL	41.57822	35.06195	976	21.47	0.16963	2.150 ± 0.086	11.202 ± 0.054	0.059 ± 0.0037
MSL	41.39891	34.50504	798	21.91	0.17002	2.104 ± 0.080	10.763 ± 0.053	0.071 ± 0.0045
YNL	41.46331	34.30093	775	21.31	0.17048	1.708 ± 0.080	8.980 ± 0.055	0.071 ± 0.0045
UTZ	41.37034	34.24751	992	21.44	0.16986	2.346 ± 0.094	12.269 ± 0.054	0.063 ± 0.0039
AZD	41.59618	33.35575	845	20.56	0.16979	4.414 ± 0.167	24.207 ± 0.057	0.028 ± 0.0018

[a] Position of sampling for detrital sands.
[b] Measurement at Cologne AMS standardized to KN01-6-2 (5.35×10^{-13}), KN01-5-3 (6.320×10^{-12}), consistent with a $1.36 \pm 0.07 \times 10^6$ yr ^{10}Be half-life.
[c] Blank corrected value; average blank $^{10}Be/^{9}Be$ value: $2.8 \times 10^{-15} \pm 5.2 \times 10^{-16}$.
[d] When calculating production rates (only for quartz-containing portions of the catchment), correction made for variations in geomagnetic field; no correction made for topographic shielding (following Di Biase et al., 2018).
[e] ^{10}Be catchment average production rates and associated denudation rates calculated using Basinga (Charreau et al., 2019), version downloaded 24.01.2020. Reference SLHL production rate: 4.11 atoms g-1 yr-1.

non-quartz minerals and remove meteoric ^{10}Be. Column chemistry and target preparation followed procedures described by von Blanckenburg et al. (2004) and Wittmann and von Blanckenburg (2016). A carrier of 150 µg of ^{9}Be was added to each sample prior to quartz digestion and isolation of $Be(OH)_2$ via column chemistry. Be was then oxidized to BeO and prepared as targets for analysis by accelerator mass spectrometry (AMS). AMS measurements were performed in July 2019 at the University of Cologne, Germany. Measured Be isotope values were normalized to the standards KN01-6-2 and KN01-5-3 with a nominal $^{10}Be/^{9}Be$ ratio of 5.35×10^{-13} and 6.32×10^{-12}, respectively. Blank corrections were performed for each sample based on the blank ratios processed with the same batch of samples ($3.56 \pm 0.64 \times 10^{-15}$ and $2.11 \pm 0.50 \times 10^{-15}$; Table 1).

We calculated catchment-average denudation rates based on the ^{10}Be concentrations in quartz with the ArcGIS toolbox Basinga (Charreau et al., 2019). ^{10}Be production rates from spallation and from muons were scaled with the Lal/Stone model from a global average sea-level high-latitude production rate of 4.11 atoms/(g×yr) based on the ERA40 atmosphere model (Martin et al., 2017), with corrections for variations in paleomagnetic intensity and the distribution of quartz-bearing rocks within the contributing catchment (Fig. S1; see Charreau et al. (2019) for details on correction procedures). We did not correct production rates for topographic shielding, following Di Biase et al. (2018). We also did not make any adjustments to production rates for snow or ice cover, as (1) the rare or thin, transient snow cover in the sampled catchments, even if they were thicker during colder Quaternary periods, likely has a minimal impact on production rates (Schildgen et al., 2005), and (2) there is no evidence that the Central Pontides were glaciated during the Quaternary. Periglacial landforms have been mapped at elevations down to 1943 m a.s.l. in the Ilgaz Range to the south (Dede et al., 2020), but there is no evidence of them in the Sinop Range.

3.2. Rock-uplift history from river profiles

For detachment-limited rivers, the change in elevation of a point along a river profile through time can be described by (Whipple and Tucker, 1999):

$$\frac{dz(t,x)}{dt} = U(t,x) - E(t,x) \tag{1}$$

where $U(t,x)$ is the rock-uplift rate, and E the erosion rate, which is defined by:

$$E = KA(x)^m S(t,x)^n \tag{2}$$

A is the upstream drainage area, S is the channel slope, K is the erosion coefficient, which is primarily related to lithology and climate, and m and n are two positive constants related respectively to basin hydrology and channel-erosion processes (Whipple and Tucker, 1999).

Eq. (2) can be solved such that:

$$S = \left(\frac{E\,(\text{or}U)}{K}\right)^{\frac{1}{n}} A^{\frac{m}{n}} \tag{3}$$

For steady-state conditions ($U = E$), no substantial changes in the drainage basin area through time (e.g., via drainage capture), and a spatially and temporally uniform K, Eq. (3) can be integrated for the upstream drainage area to predict the elevation of the river profile (Perron and Royden, 2013):

$$z(x) = z(x_b) + \left(\frac{E\,(\text{or}U)}{KA_0^m}\right)^{\frac{1}{n}} \chi \tag{4}$$

where $z(x_b)$ is the elevation of the catchment outlet and A_0 is a reference drainage area. This equation defines the χ-plot, in which χ is an integral quantity calculated from the outlet x_b to a given point x:

$$\chi(x) = \int_{x_b}^{x} \left(\frac{A_0}{A(x')} \right)^{\frac{m}{n}} dx' \quad (5)$$

Assuming $n = 1$ and block-uplift conditions, Eq. (4) can be inverted to define the non-dimensional rock-uplift rate, U^*, which is the slope of the χ-plot. U^* can be used to infer the rock-uplift (or baselevel-fall) history of a catchment (Goren et al., 2014):

$$U^* = \frac{U}{K A_0^m} \quad (6)$$

For discrete χ-intervals, imposing $z(x_b)$ equal to 0, and assuming that N data points of z and χ along the fluvial network share a common rock-uplift history (Goren et al., 2014; Gallen, 2018), Eq. (4) can be written for each data point and organized in matrix form:

$$\boldsymbol{A^* U^* = z} \quad (7)$$

where $\boldsymbol{A^*}$ is an $N \times q$ matrix, q is the number of χ intervals, $\boldsymbol{U^*}$ is the non-dimensional rock-uplift rate and $\boldsymbol{z}$ is the elevation. This is an overdetermined inverse problem, as there are more known data points than unknown parameters. As such, a least-squares estimate for $\boldsymbol{U^*}$ is used (Goren et al., 2014):

$$\boldsymbol{U^* = U^*_{pri} + (A^{*T} A^* + \Gamma^2 I)^{-1} A^{*T} (z - A^* U^*_{pri})} \quad (8)$$

where Γ is a dampening coefficient that determines the smoothness imposed on the solution, $\boldsymbol{I}$ is the $q \times q$ identity matrix and $\boldsymbol{U^*_{pri}}$ represents the prior guess for U^*. In this way, χ and U^* can be scaled for average (e.g. Goren t al., 2014) or rock-variable (e.g. Fisher et al., 2022) K to infer rock-uplift rates (U) and time (τ):

$$U = K A_0^m U^* \quad (9)$$

$$\tau = \frac{\chi}{K A_0^m} \quad (10)$$

U^*_{pri} is usually estimated by an equation that takes the average slope of the χ-plot (see Eq. (15) in Supplementary Material), but that approach can overestimate the uplift rates for the earliest stages of stream channels that record a transient response to faster rock uplift (Racano et al., 2021). When inversion results are sufficiently well resolved, results are independent of the choice of U^*_{pri}, but determining an appropriate resolution cut-off value may not be straightforward. In that case, testing different U^*_{pri} values is an easy approach to assess where exactly results are independent of U^*_{pri}. Accordingly, we propose an alternative method for the estimation of U^*_{pri}. Assuming A_0 and n equal to 1, the slope of Eq. (4) is equivalent to the river steepness index (Smith et al., 2022), which can be defined by Eq. (3):

$$U^* = \frac{E(U)}{K} = S(x)\, A(x)^{\frac{m}{n}} = k_s \quad (11)$$

We determine a best-fit m/n ratio (or "concavity index") by the χ-z plot minimization method (Goren et al., 2014; Fig. 2b). By applying the same reference m/n ratio to the whole drainage system, we can obtain the normalized steepness index (k_{sn}), which is a robust measure of relative channel steepness throughout a region (Wobus et al., 2006).

We defined U^*_{pri} as the average k_{sn} ($\pm 1\sigma$) above a chosen elevation of the inverted catchments that we call z_{prior}. This parameter was taken by considering the average elevation of a relict landscape uplifted during the last 10 Myr (∼1000 m, Ballato et al., 2018). For catchments that do not reach the elevation of the paleolandscape, or have only a small proportion of their drainage area within it, we arbitrarily set z_{prior} to the first 150 m of elevation from the channel-head of river profiles. More details about the method and the river inversion set-up are provided in the Supplementary Material.

We apply the linear inversion to 19 catchments that drain mostly perpendicular from the Sinop Range to the Black Sea. We used the MATLAB® toolbox TopoToolbox (Schwanghart and Scherler, 2014) and the ALOS 30 m DEM to extract the drainage systems and catchments, and to determine k_{sn} and χ for the river inversions. Finally, we generated spatio-temporal models of rock-uplift and uplift-acceleration by interpolating the rock-uplift histories across the single catchments with a Lowess linear smoothing function from the MATLAB® Curve Fitting Toolbox.

4. Results

4.1. Denudation rates and erosion coefficient (K) estimates

Our catchment-average denudation rates range from 0.01 to 0.3 mm/yr (Table 1). The lowest denudation rates occur in catchments that only drain the high-elevation, low-relief paleosurfaces, whereas higher rates tend to occur in catchments that include the steep, northern flank of the Sinop Range, and in two catchments within the Karabük Range (Fig. 3a).

Most of the lithological units along the Sinop Range and within the catchments sampled for ^{10}Be analysis (catchments outlined in blue in Fig. 3a and S1) comprise carbonate and clastic sedimentary rocks, whereas metamorphic rocks are exposed at the top of the Sinop Range and between catchments 5 and 10 (Fig. 2a). Most lithologies contain quartz (we only exclude carbonates without quartz or poor in quartz content, and ophiolitic rocks, Fig. S1a) and quartz-poor rocks outcrop only in limited areas (Table S1), such that in most cases, the average denudation rates can be considered representative of the full catchment upstream from the sampling points. The median and range of k_{sn} values for each lithology (Fig. 2c) do not show strong variations, except for the volcanic and clastic rocks, limestones and marbles, which show the widest range of values, but never more than 2x greater than the others (Table S2).

Considering the definition of the steepness index, i.e., $k_{sn} = (E/K)_{1/n}$, a linear regression between k_{sn} and denudation rate, E, yields a plot with a slope equal to K (i.e., $E = K \times k_{sn}^n$). If n were much different from 1, the plot of E versus k_{sn} would be nonlinear. We find a positive, linear correlation between catchment-average denudation rates and catchment-average k_{sn} values (based on a best-fit concavity index of 0.5, Fig. 2b) of quartz-bearing lithologies ($R^2 = 0.74$ or 0.76; Fig. 3b and Fig S2), which supports the assumption of $n = 1$ (see also Fig. S1c) needed to apply the linear inversion and to estimate K from Eq. (11) (Fig. 3). Points that fall farther from this linear trend show no systematic characteristics (such as percentage of crystalline versus sedimentary rocks in the catchment, Fig. S2, or average annual rainfall) that we were able to discern. The lack of systematic differences in this trend between predominantly crystalline and predominantly sedimentary (including carbonate) rocks (Fig. S2) suggests that carbonate dissolution within the source catchments, which would have the effect of slowing the exhumation of quartz-bearing lithic fragments or quartz grains (e.g., Riebe et al., 2021; Ott et al., 2022), does not have a strong influence on our denudation rates. However, the samples from the western Sinop Range (diamonds in Fig. 3) follow a steeper trend than those from the central/eastern Sinop Range (circles) and from the Kastamonu and Boyabat basins (squares), potentially suggesting changes in K toward the west. For this reason, we performed two different linear regressions on the denudation rate versus k_{sn} plot, including and excluding the four westernmost sampled catchments. We respectively obtained

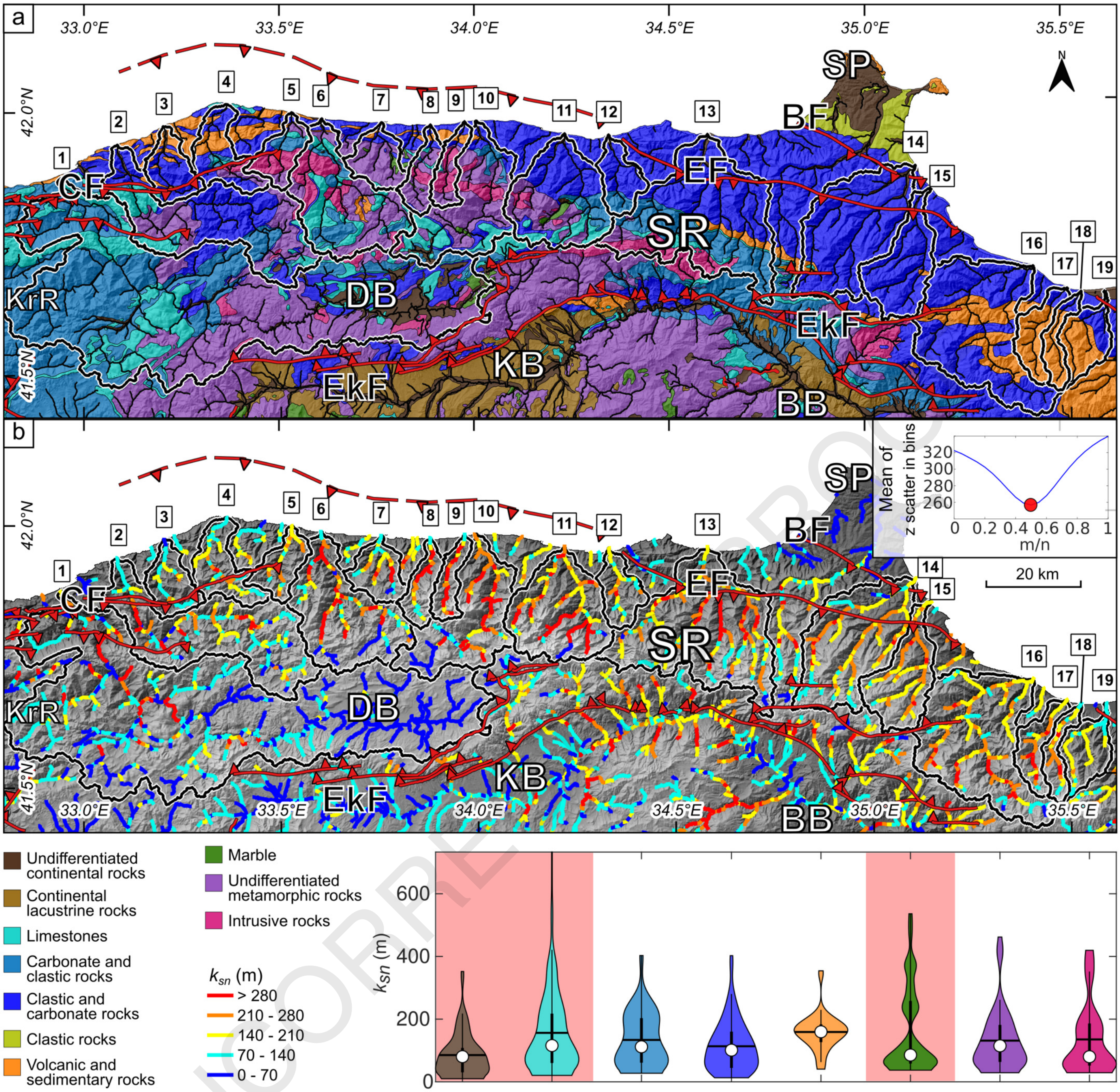

Fig. 2. Comparison of rock types and steepness values in the Central Pontides. (a) Lithological map of the Sinop Range. (b) Normalized steepness index (k_{sn}) map of the Sinop Range and estimation of the best fit concavity index (m/n). (c) Violin plots of the k_{sn} values for every outcropping lithology in the catchments for which river-profile inversions were performed, outlined in black in a and b; white dot and black horizontal line inside the violins indicate respectively the median and the mean k_{sn}, pink bands indicate the lithologies that do not contain substantial quartz content.

two K values of 5.4×10^{-7} ($1\sigma = 2.4 \times 10^{-8}$) and 5.1×10^{-7} ($1\sigma = 2.6 \times 10^{-8}$) $m^{0.4}$/yr. (Fig. 3b). The average of K values estimated individually for every sampled catchment (Fig. 3c) is 6.0×10^{-7} ($1\sigma = 1.05 \times 10^{-7}$) $m^{0.4}$/yr. Western catchments show more variable K values compared to the eastern catchments, which tend to fall close to 5.6×10^{-7} ($1\sigma = 7.5 \times 10^{-8}$) $m^{0.4}$/yr.

In general, the mean values of K obtained from linear regression and from the average of single catchments fall inside the ranges of K values estimated for each quartz-bearing lithology, with values around $\sim 5 \times 10^{-7}$ $m^{0.4}$/yr more representative or metamorphic and volcanic rocks and values of $\sim 6 \times 10^{-7}$ $m^{0.4}$/yr closer to volcanic/sedimentary and intrusive rocks (Table S2).

4.2. Non-dimensionalized river-profile inversion results

Our river-profile inversions show for most of the analyzed catchments minor differences between real and modeled river elevations, with results being generally within ±50 m (Fig. S3) and average modeled χ-plots reflecting well the average trend of real χ-plots from the analyzed catchments.

Most of the U^* (non-dimensionalized rock-uplift rate) curves show an increasing trend with peak values reached in most cases at χ values between 1500 and 4000 m, and then a general decrease moving towards $\chi = 0$ m. Only for catchments 1, 2 and 6, the highest values of U^* are reached for χ values equal or close to zero (Fig. 4a).

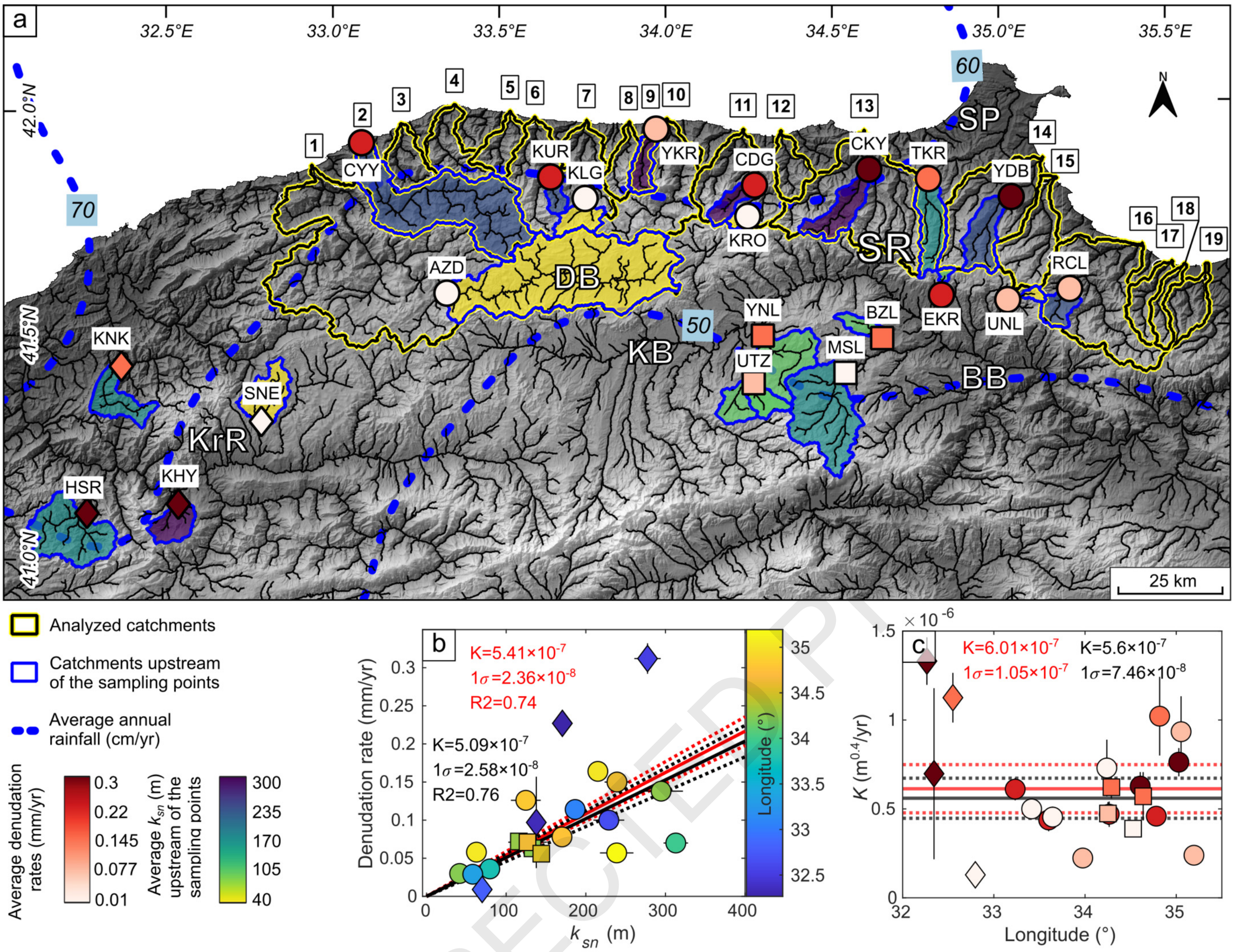

Fig. 3. Analysis of erodibility parameter K. (a) Location of the sampling points of the detrital sands for ^{10}Be analysis (color-coded by denudation rate and labeled with a three-letter sample code), and associated catchments (color-coded by average k_{sn} in quartz-bearing rocks upstream from the sampling points). Circles indicate the sampling points along the Sinop Range, squares the sampling points between the Kastamonu and Boyabat Basins, diamonds the sampling points in the Karabük Range (KrR). (b) K estimation from a York regression forced through the origin of the average k_{sn} upstream of the sampling points versus the estimated denudation rates. In red: the regression performed considering all the sampling points; in black: the regression performed excluding the four westernmost points (diamonds). (c) Erodibility parameter (K) estimated individually for each sampling point by dividing the denudation rate by the upstream average k_{sn}. The average K values have been estimated with (red) and without (black) the sampling locations in the Karabük Range. The points are colored following the relative denudation rate.

The differences in U^* trends obtained by imposing the average k_{sn} ($\pm 1\sigma$) above z_{prior} as U^*_{pri} generally affects the earliest step of the inversions (Fig. 4a), suggesting a stronger dependency on U^*_{pri}. However, the chosen U^*_{pri} value does not have a substantial impact on the average U^* trends or on the modeled χ-plots (Fig. 4a). Moreover, by applying the inversion for $U^*_{pri} = k_{sn} + 1\sigma$ or $k_{sn} - 1\sigma$ above z_{prior}, the difference between the modeled elevations compared with the ones obtained for $U^*_{pri} = k_{sn}$, and also the misfit between real and modeled elevations, is very low (Fig. 4b).

5. Discussion

5.1. Reliability and limits of the river-profile inversions

Comparing our approach for the selection of U^*_{pri} (using the average k_{sn} above z_{prior}) with the one based on Eq. (15) (see supplementary material), we did not find major differences in the average misfit between real and modeled river profiles and in the average uplift trends (Figs. S4b, S5, S6, S7). However, our approach tends to yield lower rock-uplift rates in the earliest time steps (Fig. S4a), which is consistent with earlier suggestions that rock-uplift rates were generally low prior to the most recent late Miocene to Pliocene acceleration (e.g., Yildirim et al., 2011; Ballato et al., 2018). Nevertheless, the variation in inferred rock-uplift rates for those earliest time steps when using the different U^*_{pri} estimates illustrates that those time intervals are not well resolved, and should be removed from further interpretation, as we have done (Fig. 4).

The block-uplift condition could be potentially complicated by the presence of thrust faults that cut some of the inverted catchments (for instance catchments 2, 3 and 4 crossed by CF and catchments 13, 14 and 15 cut by the EF) (Fig. 2). However, there are no major differences in the inversion results compared to their neighboring catchments that are not crossed by the faults, suggesting that over the investigated timescale, the rock-uplift history of the range may be mainly accommodated by faults located farther north (e.g. Black Sea Fault, Fig. 1b).

The effects of stationary knickpoints (e.g. lithological knickpoints) can impact the inversion results substantially. Catchments 1, 2 and 6 show U^* trends that appear to be affected by lithologic

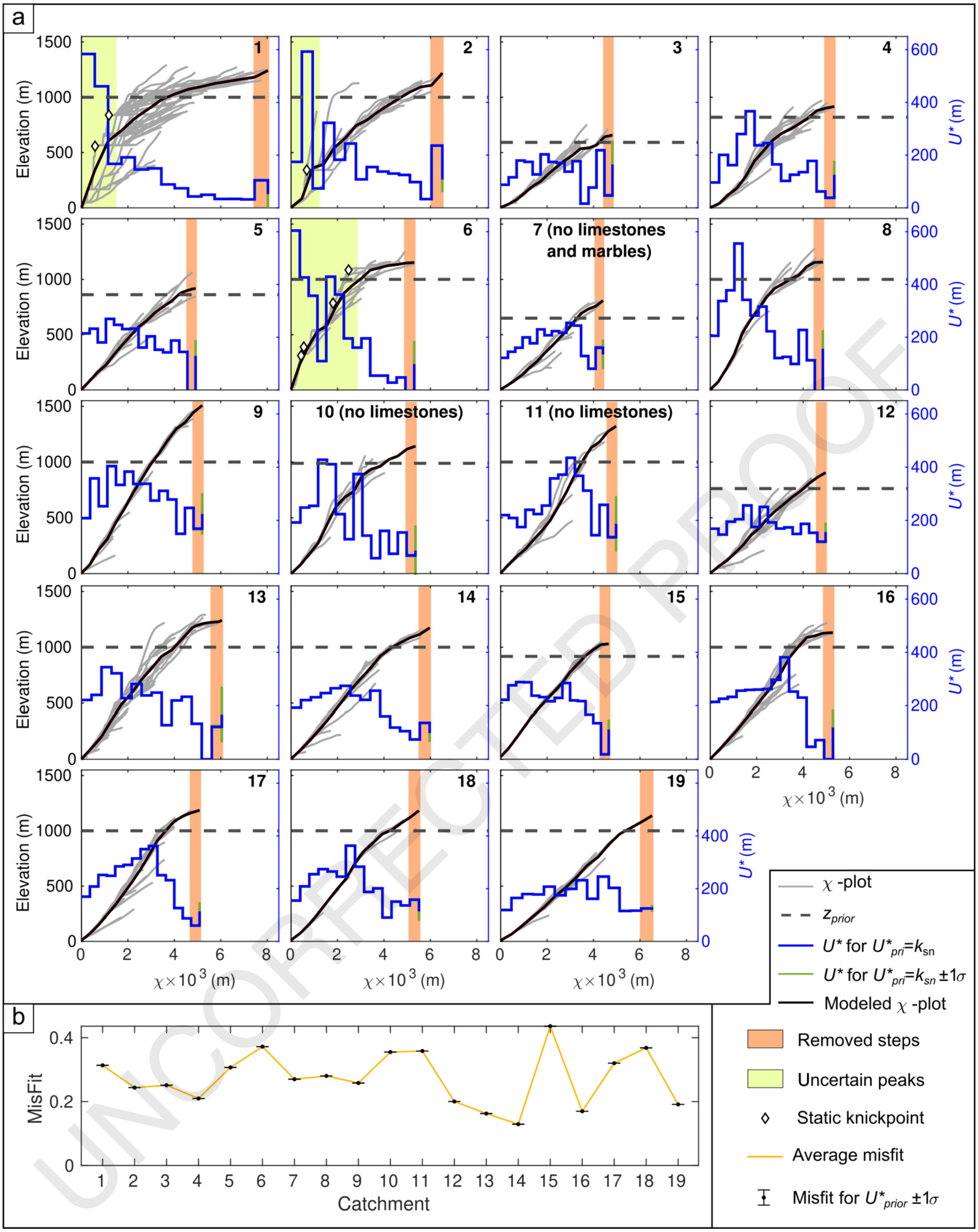

Fig. 4. Non-dimensional results of river-profile inversions. (a) Non-dimensional linear inversion of 19 catchments draining to the Black Sea. The thin gray lines are the chi-plots for all the tributaries in the catchment, the thick black line is the modeled chi-plot, and the red lines are the uncertainties of the modeled elevations obtained for $U^*_{pri} \pm 1\sigma$. The blue thick lines are the modeled U^*, and the green ones $\pm 1\sigma$. The dashed line indicates the limit of the z_{prior}. The greenish areas are the uncertain U^* peaks, while the orange ones indicate the bad resolved steps that have been excluded for the estimation of the rock uplift; more details are discussed in the text and in Figs. S11 and S12. (b) Inversion misfit obtained for U^*_{pri} equal to the mean k_{sn} ($\pm 1\sigma$) above z_{prior}.

variations. In more detail, the inversions for catchments 1, 2, and 6 show a continuous increase in U^*, which is substantially different from the other river profiles, with a strong and continuous increase from around $\chi \sim 2000$ m to the catchment outlets (Fig. 4). The jumps in U^* recorded from $\chi \sim 2000$ m can be associated with a lithological knickpoint at the boundary between limestones and clastic and carbonate rocks in catchment 1 and between limestones and crystalline rocks in catchments 2 and 6 (Fig. S11).

In catchments 7, 10 and 11, limestones and marbles are exposed mainly in areas close to the watershed divides (Fig. 2a). In these cases, the inversion results show big U^* peaks for the higher χ values (catchments 7 and 11), or large $U^* \pm 1\sigma$ ranges that generate negative non-dimensional rock-uplift rates (catchments 10 and 11) (Fig. S12). However, by excluding from the catchments the areas where limestones and marbles are exposed, the U^* curves obtained are more concordant with the inversion results of catchments where these lithologies have no or limited exposure.

The effect of lithological variations can be mitigated by inverting rivers for rock-variable K (Gallen, 2018; Fisher et al., 2022). To apply rock-variable K inversion two further assumptions are needed: (a) rock unit contacts are stationary through time, and (b) the erodibility of all the rocks crossed by inverted stream channels is known. The first assumption is valid only if rock limits are vertical or dipping at a high angle, or if the investigated time frame is short enough to consider rock-limit migration negligible. In our study case, both of these assumptions cannot be satisfied, because the steady position of rock limits over 10 Myr is unlikely, and we cannot estimate K for rocks with poor or no quartz content (limestones and marbles). Regardless, even when using variable estimates of K for limestones and marbles (based on their mean k_{sn} values) to test the effect of rock-variable K on river inversions (Fig. S13), we did not find substantial differences in the rock-uplift histories compared to those obtained by using a single, average K (Fig. S14).

5.2. Spatio-temporal pattern of denudation and rock uplift

Our ^{10}Be derived denudation rates, which show lowest values for catchments that primarily drain the low-relief, high-elevation surfaces and highest values for catchments along the steep, northern flank of the Sinop Range, suggest a transient adjustment of the landscape to increased rock-uplift rates. Our river profile inversions enable us to utilize those transient forms to quantitatively constrain the onset of faster rock-uplift.

The rock-uplift rates obtained by scaling U^* for the four estimated $K \pm 1\sigma$ values show uplift trends quite concordant in timing and variations, and most of the curves tend to concentrate around the median values (Fig. S14). This minimum variability suggests that our estimate of K is well determined.

Most of the rivers whose catchments drain the paleosurface (10, 11, 13, 14, 15 and 16) show a rock-uplift history spanning at least the last 10 Myr (Fig. 5c-d). The average rock-uplift trend for most of the analyzed catchments shows a peak in rock-uplift rates between 2.5 and 6 Ma, reaching values between 0.2 and 0.3 km/Myr (Fig. S14). Moreover, all rock-uplift and uplift-acceleration histories indicate an important rock-uplift phase that started between ∼10 and 7.5 Ma (Fig. 5d). Around ∼3 to 2 Ma, rock-uplift rates started to decelerate, a trend that continues until the present. Some parts of the rock-uplift model lack data to better reconstruct the spatio-temporal variation of rock uplift, such as near the Sinop Peninsula. However, the modeled rock-uplift rates for the younger stages (last 0.6 Myr) are in good agreement with estimates of the Quaternary rock-uplift rates inferred from dated marine terraces in that region (Yildirim et al., 2013b, Fig. 5a), supporting the reliability of our inversion results.

The rock-uplift and uplift-acceleration models (Fig. 5c, d) illustrate that the onset of accelerated rock-uplift is not synchronous along the Sinop Range, but rather follows an east-to-west propagation pattern. On the eastern side (between catchments 14 and 19), rock-uplift started to accelerate around 10 Ma, whereas on the western side (catchments 3, 4, 5), the acceleration started around 7.5 Ma. Stronger smoothing in the interpolation has minor effects on these results. For example, smoother interpolations reveal clear east-to-west migration in rock-uplift rates and uplift-acceleration from ∼10 to 7.5 Ma, with a deceleration of rock-uplift rates synchronously along the whole Sinop Range starting from ∼2 Ma (Fig. S15).

5.3. Inferred timing and rates of NAF westward propagation

Analogue experiments of transpressive systems (e.g. Leever et al., 2011; Barcos et al., 2016) have shown that for a low angle (e.g., <5°, Leever et al., 2011) between the convergence velocity vector and the deforming margin, tectonic strain is highly localized and is associated with the development of a single strike-slip fault parallel to the margin. Conversely, when obliquity is greater (e.g., >7.5° Leever et al., 2011), convergence is absorbed through the development of a wide, contraction-dominated deformation wedge consisting of thrust and strike-slip faults subparallel to oblique (up to 40°) to the margin. This type of margin typically follows an evolution that can be summarized in three kinematic stages (Leever et al., 2011): an initial phase where strain is accommodated without faulting ("distributed strain"); a second phase with the development of faults accommodating oblique slip ("oblique wedge"); and a final phase where the strain becomes partitioned into strike-slip faulting along a narrow master fault and dip-slip faulting along branching reverse faults ("strain partitioning").

The NAF in the Central Pontides represents an example of a contraction-dominated transpressive margin. There, the convergence angle between the Anatolian micro-plate and the Black Sea inferred from GPS data varies from <5 to ∼18° (Fig. 6b). This variation is thought to induce strain partitioning, with right-lateral strike-slip faulting along the NAF and thrusting along late Cretaceous normal faults reactivated in late Miocene to Pliocene times (Yildirim et al., 2011; Espurt et al., 2014; Ballato et al., 2018).

In this context, we interpret accelerated rock uplift along the Sinop Range as the onset of the "strain partitioning stage", when the Ekinveren Fault started accommodating dip-slip (thrusting) motion away from the NAF. This interpretation agrees with low-temperature thermochronological data, which document a post 11 Ma phase of fault-related exhumation (Ballato et al., 2018). If correct, the westward propagation of faulting along the Sinop Range should be coeval with or shortly postdate the inception of the NAF in the Central Pontides. The good agreement between our timing estimates and the late Miocene to Pliocene age of the sediments preserved in the transpressional basins adjacent to the NAF (Barka and Hancock, 1984) suggest a link between uplift in the Sinop Range and faulting along the NAF that also matches the predictions of analogue models (e.g., Barcos et al., 2016).

The location of the fastest rock-uplift rates inferred from our inversions broadly coincides with the highest topography in the Sinop Range (Fig. 5b, c) and the greatest exhumation based on low-temperature thermochronometry (Ballato et al., 2018). The location of the maximum rock-uplift rates appears to be controlled to a first-order by the arc-shaped geometry of the NAF and its obliquity with respect to the plate convergence vectors (Yildirim et al., 2011). Why rock-uplift rates increased and then decreased with time, however, is unclear. One possibility is that contractional deformation started to be accommodated offshore, in association with the widening of the transpressive orogenic wedge. This hypothesis is consistent with seismic and multibeam bathymetry data documenting the occurrence of E-W oriented reverse faults and minor right-lateral strike slip faults cutting supposed Plio-Pleistocene offshore strata (İşcan et al., 2019). Additional evidence for the widening of the transpressive wedge comes from the strongest instrumentally recorded compressive earthquake that occurred along the southern margin of the Black Sea in 1968 (Bartin earthquake; Alptekin et al., 1986).

Finally, we can consider our results in the context of long-term westward propagation of the NAF from the Eastern Pontides to the Marmara Sea, based on estimated ages for the onset of NAF

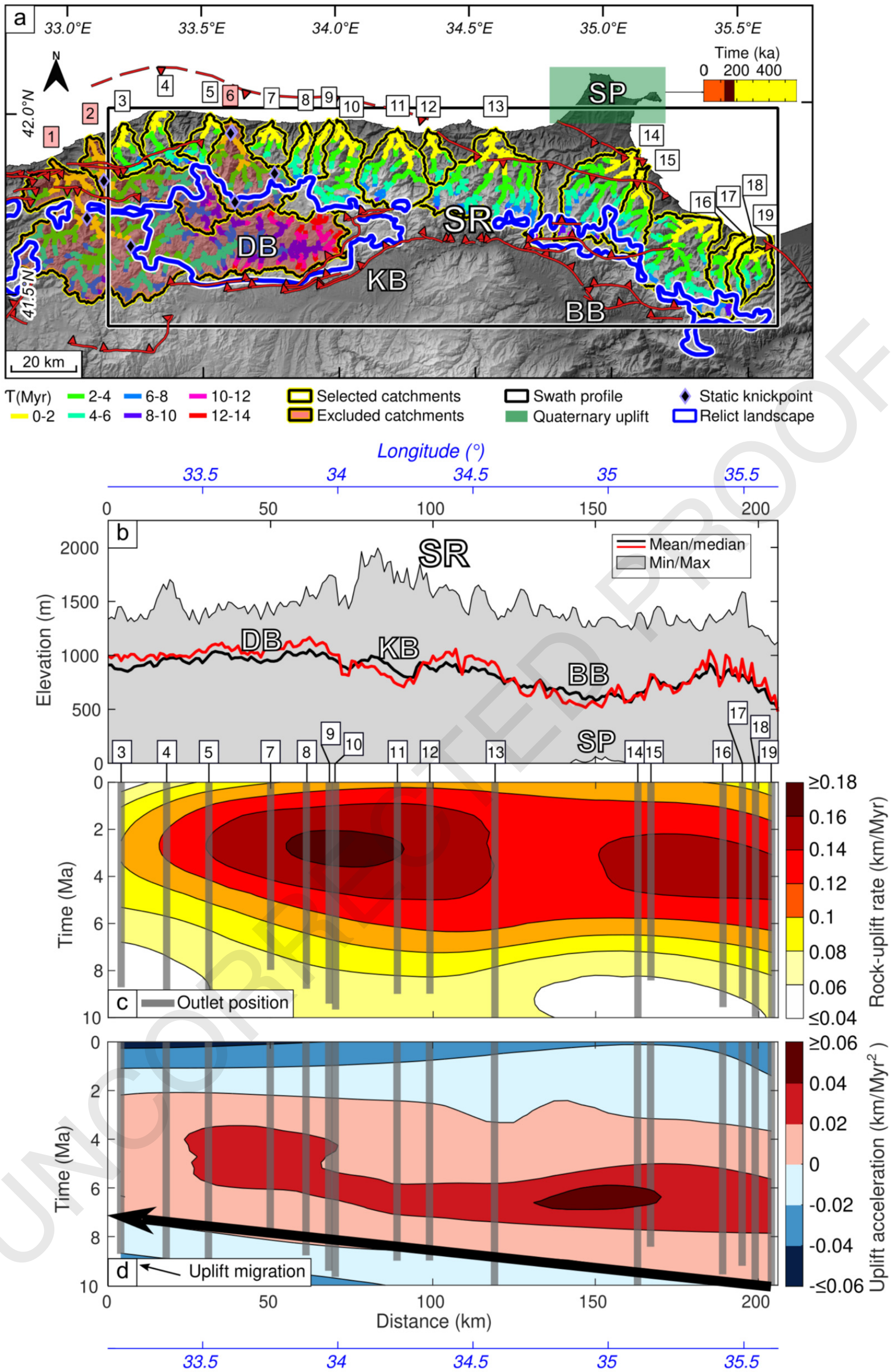

Fig. 5. (a) τ-map of the inverted catchments in the Sinop Range, location of the relict landscape identified in Yildirim et al. (2011) and Ballato et al. (2018), trace of the swath profile in (b) and rock-uplift rates on the Sinop Peninsula from Yildirim et al. (2013a, 2013b) (values of rock-uplift given in (c)); the catchments highlighted in pink are the ones excluded from the final analysis because of the presence of stationary knickpoints. (b) Swath profile of the Sinop Range, and position of the outlet of the catchments used to generate the rock uplift (c) and uplift acceleration (d) models. (c) Spatio-temporal model of rock-uplift rates in the Sinop Range inferred by spatially interpolating the uplift histories of the single catchments. Thick gray lines indicate the average longitudinal position of the catchment outlets used for the inversions, with the length of the line indicating how far back in time the rock-uplift history for each catchment extends. The model shown in the figure was obtained by applying a lowess linear smoothing function with a span of 0.50. In Fig. S15, we show how the smoothing of the solution and the model changes by varying the span values. (d) Spatio-temporal uplift acceleration model along the Sinop Range (first derivative of the map in (c)). The dashed black arrow indicates the migration of the onset of faster uplift through time.

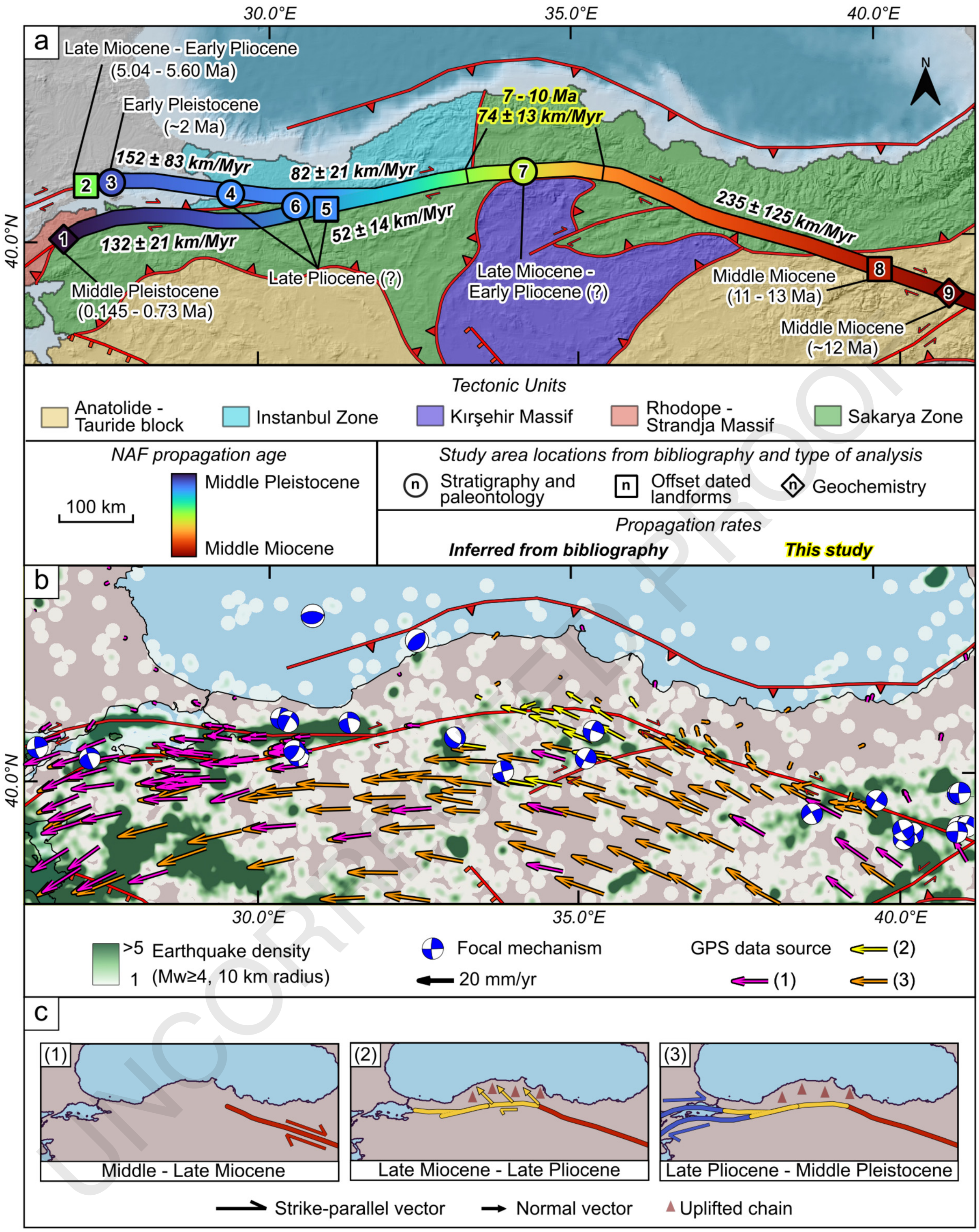

Fig. 6. (a) Main tectonic units of the Anatolian Plate (modified from Yolsal-Çevikbilen et al., 2012) and propagation history of the North Anatolian Fault (NAF) inferred from the literature and this analysis, with estimated propagation rates. The locations of the study areas from other papers have been classified following the type of analysis (shape of the point) and the inferred age for the arrival of the fault (color). The numbers inside the points indicate the references of the study: (1) Karabacak et al., 2021; (2) Karakaş et al., 2018; (3) Le Pichon et al., 2016; (4) Alpar and Yaltırak, 2002; (5) Yıldırım and Tüysüz, 2017; (6) Ünay et al., 2001; (7) Barka and Hancock, 1984; (8) Şengör et al., 2005; (9) Hubert-Ferrari et al., 2009. The color gradient of the fault follows the inferred propagation time. (b) GPS velocities, earthquake distribution in the Anatolian Plate and focal mechanisms of the main earthquakes (magnitude >5.5, from the CGMT catalogue [Ekström et al., 2012], and from Alptekin et al., 1986). GPS velocities are from three different catalogs: (1) Reilinger et al., 2006; (2) Yavaşoğlu et al., 2011; (3) England et al., 2016. The earthquake density map is based on the location of all earthquakes with a magnitude >4 recorded between the 1970 and the 2022 (USGS database). The map was created counting the number of earthquakes inside a circular sliding averaging window of 10 km. (c) Model proposed for the propagation of the NAF and the uplift of the Central Pontides. The model is divided into three stages: (1, red) nucleation and westward migration of the NAF through the Eastern Pontides; (2, yellow) propagation of the NAF through the Central Pontides, with partitioning of strain inducing uplift of the Central Pontides (brown triangles); (3, blue) acceleration of westward propagation of the NAF through the Marmara Sea. The length of the strike-slip vectors is qualitatively proportional to the magnitude of the propagation.

activity in different regions (Fig. 6a). The average westward propagation rate from the easternmost sectors of the NAF at ∼12 Ma to the west side of the Marmara Sea at ∼2 Ma, over the 1210-km length of the fault in this region, is ∼121 km/Myr. In more detail, the propagation rate from the easternmost sectors of the NAF to the Central Pontides (511 km), from ∼12 to ∼10 Ma, was 235 ± 125 km/Myr. This high degree of uncertainty for the eastern segment is due to the limited age constraints available to calculate the propagation rate relative to the segment length, and the fact that the ages are clustered near the eastern tip of the fault. In the Central Pontides, we infer a westward propagation of ∼220 km from ∼10 to ∼7 Ma, at 74 ± 13 km/Myr. From the western edge of the Central Pontides (∼33°E), the NAF runs westward for ∼115 km and then splits into two branches. The northern branch propagated ∼200 km from the triple junction to the Marmara Sea (point 4, Fig. 5a), with a total length of ∼315 km from ∼7 to ∼3 Ma at 82 ± 21 km/Myr. The southern branch propagated for ∼200 km (from Central Pontides to point 6, Fig. 6a) at 52 ± 14 km/Myr. Finally, although for the Marmara Sea different estimates exist, the NAF most likely propagated ∼165 km from ∼3 to ∼2 Ma along the northern branch and ∼350 km from ∼3 to ∼0.73 or 0.145 Ma along the southern branch, respectively at rates of 152 ± 83 km/Myr and 132 ± 21 km/Myr. These apparent variations in fault propagation rates of the NAF derived from individual segments could be linked to rheologic and/or geometric variations. The propagation rates of segments with an ESE-WNW orientation appear to be roughly twice as fast as those oriented E-W or ENE-WSW, suggesting that the segments associated with greater strain partitioning and transpression (i.e., along the Central Pontides; Yildirim et al., 2011) may have slowed the westward propagation of the NAF. Even today, focal mechanisms of recent earthquakes (Fig. 6b) suggest that strike-slip faulting is not well concentrated along the central sector of the NAF, unlike the sectors to the west and east (Yolsal-Çevikbilen et al., 2012, Fig. 6b). The central segment is partly delimited to the south by the Kırşehir Massif, a thick, high-rigidity continental block embedded between the Anatolide–Tauride and Sakarya blocks (Şengör and Yilmaz, 1981, Fig. 6a). This coincidence, with the NAF wrapping northward around this rigid block, suggests that the underlying geology played an important role in the geometry and evolution of the NAF.

Accordingly, we summarize the history of NAF propagation in three main stages (Fig. 6c):

(1) From middle to late Miocene time, the NAF formed through localization of strain within the North Anatolian Fault Zone in eastern Turkey, migrating westward at ∼235 km/Myr in an ESE-WNW direction;

(2) In the late Miocene, the propagation velocity of the NAF decreased to ∼74 km/Myr along segment(s) oriented WSW-ENE in central Turkey. Greater obliquity of convergence between the Anatolian and Eurasian plates induced transpression to the north of the NAF and accelerated rock uplift in the Central Pontides. During the late Pliocene, the NAF propagated to the Marmara Sea along two branches: a southern branch (∼52 km/Myr) and a northern branch (∼82 km/Myr);

(3) After the Pliocene, the NAF propagated westward along segments oriented E-W to ESE-WNW through western Turkey and the Marmara Sea. With obliquity to plate-convergence vectors reduced, the stresses became localized again along the shear zone and westward propagation rates accelerated to ∼132 to 152 km/Myr. Rock-uplift rates started to decelerate in the Sinop Range around late Pliocene to early Pleistocene time, potentially associated with outward growth of the Central Pontide orogenic belt.

6. Conclusions

Our geomorphometric analysis of rivers draining the Sinop Range, together with 21 new ^{10}Be derived denudation rates from catchments, provides important new constraints on the rock-uplift history of the northern margin of the Central Pontides. Linear inversions of the river profiles indicate that the area underwent an accelerated rock-uplift phase during the last 10 Myr, and they allow us to define its rates and temporal variations. Peak rock-uplift rates averaged between 0.15 and 0.25 km/Myr, with the fastest uplift occurring in the western part of the Sinop Range, where the chain currently reaches the highest elevations. Furthermore, we find that the onset of faster uplift within the Central Pontides was not synchronous along the chain, but rather propagated westward at a rate of ∼74 km/Myr. Rock-uplift rates then began to decelerate at ∼2 Ma, almost simultaneously across the study area. Considering the predicted close relationship between the uplift of the Central Pontides and the transpressive stresses generated along the central NAF segments, we interpret the westward migration of faster rock uplift as concomitant with the westward propagation of the NAF.

Combining our results with those obtained from the literature, we illustrate the age and propagation rates of the NAF from its origin in eastern Turkey to the Marmara Sea. This analysis reveals strong differences in propagation rates between the central NAF segment (∼74 km/Myr), the older eastern segment (∼235 km/Myr), and the two younger western segments (∼82 to 152 km/Myr for the northern branch, and 52 to 132 km/Myr for the southern branch). Differences in the orientation of the NAF relative to the regional plate convergence vector, potentially controlled by the underlying geology, may explain these variable fault-propagation rates: segments that are more strongly oblique to the plate convergence vectors, which are associated with stronger strain partitioning and transpression, show slower propagation rates compared to segments oriented more parallel to the convergence vectors.

Declaration of competing interest

The authors declare that they have no known competing financial interests or personal relationships that could have appeared to influence the work reported in this paper.

Data availability

The code used to perform river linear inversion is a modified version of the code used in Pavano and Gallen (2021). The library of MATLAB functions used for river linear inversion analysis is freely available, with open-access, at https://doi.org/10.5281/zenodo.7577077.

Acknowledgements

This study was started as part of the Anatolian Plateau Climate and Tectonic Hazards (ALErT) project, funded by the European Union Marie Curie Actions “Innovative Training Networks” program (FP7-PEOPLE-2013-ITN, grant agreement 607996). We thank Görkem Sivri for help with field work and sample processing. PB was supported by the MIUR (Italian Ministry of Education University and Research) through the Excellence Department Initiative (Art. 1, com. 314-337, Low 232/2016) and the PRIN 2017-2020 funding scheme (project: Geodynamics of the Arabia-Eurasia collisional zones, PI C. Faccenna).

Appendix A. Supplementary material

Supplementary material related to this article can be found online at https://doi.org/10.1016/j.epsl.2023.118231.

References

Alpar, B., Yaltırak, C., 2002. Characteristic features of the North Anatolian Fault in the eastern Marmara region and its tectonic evolution. Mar. Geol. 190, 329–350. https://doi.org/10.1016/S0025-3227(02)00353-5.

Alptekin, Ö., Nábělek, J.L., Toksöz, M.N., 1986. Source mechanism of the Bartin earthquake of September 3, 1968 in northwestern Turkey: evidence for active thrust faulting at the southern Black Sea margin. Tectonophysics 122, 73–88. https://doi.org/10.1016/0040-1951(86)90159-9.

Ballato, P., Parra, M., Schildgen, T.F., Dunkl, I., Yıldırım, C., Özsayı, n E., Sobel, E.R., Echtler, H., Strecker, M.R., 2018. Multiple exhumation phases in the Central Pontides (N Turkey): new temporal constraints on major geodynamic changes associated with the closure of the Neo-Tethys Ocean. Tectonics 37, 1831–1857. https://doi.org/10.1029/2017TC004808.

Barcos, L., Díaz-Azpiroz, M., Balanyá, J.C., Expósito, I., Jiménez-Bonilla, A., Faccenna, C., 2016. Analogue modelling of inclined, brittle–ductile transpression: testing analytical models through natural shear zones (external Betics). Tectonophysics 682, 169–185. https://doi.org/10.1016/j.tecto.2016.05.021.

Barka, A.A., Hancock, P.L., 1984. Neotectonic deformation patterns in the convex-northwards arc of the North Anatolian fault zone. Geol. Soc. (Lond.) Spec. Publ. 17, 763–774. https://doi.org/10.1144/GSL.SP.1984.017.01.61.

Berndt, C., Yıldırım, C., Çiner, A., Strecker, M.R., Ertunç, G., Sarıkaya, M.A., Özcan, O., Ozturk, T., Kiyak, N.G., 2018. Quaternary uplift of the northern margin of the Central Anatolian Plateau: new OSL dates of fluvial and delta-terrace deposits of the Kızılırmak River, Black Sea coast, Turkey. Quat. Sci. Rev. 201, 446–469. https://doi.org/10.1016/j.quascirev.2018.10.029.

Charreau, J., Blard, P.-H., Zumaque, J., Martin, L.C.P., Delobel, T., Safran, L., 2019. Basinga: a cell-by-cell GIS toolbox for computing basin average scaling factors, cosmogenic production rates and denudation rates. Earth Surf. Process. Landf. 44, 2349–2365. https://doi.org/10.1002/esp.4649.

Dede, V., Dengiz, O., Demirağ Turan, I., Türkeş, M., Gökçe, C., Serin, S., 2020. Determination of some relationships between soil erodibility properties and physiochemical of soils formed on various periglacial landforms in Ilgaz Mountains. Turkish J. Geogr. Sci. 18 (1), 99.123. https://doi.org/10.33688/aucbd.689755.

Di Biase, R.A., Denn, A.R., Bierman, P.R., Kirby, E., West, N., Hidy, A.J., 2018. Stratigraphic control of landscape response to base-level fall, Young Womans Creek, Pennsylvania, USA. Earth Planet. Sci. Lett. 504, 163–173. https://doi.org/10.1016/j.epsl.2018.10.005.

Ekström, G., Nettles, M., Dziewoński, A.M., 2012. The global CMT project 2004–2010: centroid-moment tensors for 13,017 earthquakes. Phys. Earth Planet. Inter. 200–201, 1–9. https://doi.org/10.1016/j.pepi.2012.04.002.

England, P., Houseman, G., Nocquet, J.-M., 2016. Constraints from GPS measurements on the dynamics of deformation in Anatolia and the Aegean: dynamics of Anatolia and the Aegean. J. Geophys. Res., Solid Earth 121, 8888–8916. https://doi.org/10.1002/2016JB013382.

Espurt, N., Hippolyte, J.-C., Kaymakci, N., Sangu, E., 2014. Lithospheric structural control on inversion of the southern margin of the Black Sea Basin, Central Pontides, Turkey. Lithosphere 6, 26–34. https://doi.org/10.1130/L316.1.

Fisher, J.A., Pazzaglia, F.J., Anastasio, D.J., Gallen, S.F., 2022. Linear inversion of fluvial topography in the northern Apennines: comparison of base-level fall to crustal shortening. Tectonics 41, e2022TC007379. https://doi.org/10.1029/2022TC007379.

Gallen, S.F., 2018. Lithologic controls on landscape dynamics and aquatic species evolution in post-orogenic mountains. Earth Planet. Sci. Lett. 493, 150–160. https://doi.org/10.1016/j.epsl.2018.04.029.

Goren, L., Fox, M., Willett, S.D., 2014. Tectonics from fluvial topography using formal linear inversion: theory and applications to the Inyo Mountains, California. J. Geophys. Res., Earth Surf. 119, 1651–1681. https://doi.org/10.1002/2014JF003079.

Hubert-Ferrari, A., Armijo, R., King, G., Meyer, B., Barka, A., 2002. Morphology, displacement, and slip rates along the North Anatolian Fault, Turkey: the North Anatolian Fault. J. Geophys. Res. 107. https://doi.org/10.1029/2001JB000393. ETG 9-1-ETG 9-33.

İşcan, Y., Ocakoğlu, N., Kılıç, F., Özel, O., 2019. Active tectonics of offshore Cide–Sinop (southern Black Sea shelf): from seismic and multibeam bathymetry data. Geo Mar. Lett. 39, 279–294. https://doi.org/10.1007/s00367-019-00572-4.

Karabacak, V., Sançar, T., Yildirim, G., Uysal, I.T., 2021. When did the North Anatolian fault reach southern Marmara, Turkey?. Geology 50, 432–436. https://doi.org/10.1130/G49726.1.

Karakaş, Ç., Armijo, R., Lacassin, R., Suc, J.-P., Melinte-Dobrinescu, M.C., 2018. Crustal strain in the Marmara pull-apart region associated with the propagation process of the North Anatolian Fault. Tectonics 37, 1507–1523. https://doi.org/10.1029/2017TC004636.

Koç, A., Kaymakci, N., van Hinsbergen, D.J.J., Kuiper, K.F., Vissers, R.L.M., 2012. Tectono-Sedimentary evolution and geochronology of the Middle Miocene Altınapa Basin, and implications for the Late Cenozoic uplift history of the Taurides, southern Turkey. Tectonophysics 532–535, 134–155. https://doi.org/10.1016/j.tecto.2012.01.028.

Koçyiğit, A., Yilmaz, A., Adamia, S., Kuloshvili, S., 2001. Neotectonics of East Anatolian Plateau (Turkey) and Lesser Caucasus: implication for transition from thrusting to strike-slip faulting. Geodin. Acta 14, 177–195. https://doi.org/10.1080/09853111.2001.11432443.

Krystopowicz, N.J., Schoenbohm, L.M., Rimando, J., Brocard, G., Rojay, B., 2020. Tectonic geomorphology and Plio-Quaternary structural evolution of the Tuzgölü fault zone, Turkey: implications for deformation in the interior of the Central Anatolian Plateau. Geosphere 16 (5), 1107–1124. https://doi.org/10.1130/GES02175.1.

Le Pichon, X., Şengör, A.M.C., Kende, J., İmren, C., Henry, P., Grall, C., Karabulut, H., 2016. Propagation of a strike-slip plate boundary within an extensional environment: the westward propagation of the North Anatolian Fault. Can. J. Earth Sci. 53, 1416–1439. https://doi.org/10.1139/cjes-2015-0129.

Leever, K.A., Gabrielsen, R.H., Faleide, J.I., Braathen, A., 2011. A transpressional origin for the West Spitsbergen fold-and-thrust belt: insight from analog modeling. Tectonics 30. https://doi.org/10.1029/2010TC002753.

Martin, L.C.P., Blard, P.-H., Balco, G., Lavé, J., Delunel, R., Lifton, N., Laurent, V., 2017. The CREp program and the ICE-D production rate calibration database: a fully parameterizable and updated online tool to compute cosmic-ray exposure ages. Quat. Geochronol. 38, 25–49. https://doi.org/10.1016/j.quageo.2016.11.006.

Mazzini, I., Hudácková, N., Joniak, P., Kovácová, M., Mikes, T., Mulch, A., Rojay, F.B., Lucifora, S., Esu, D., Soulié-Märsche, İ., 2013. Palaeoenvironmental and chronological constraints on the Tuğlu Formation (ÇankırıBasin, Central Anatolia, Turkey). Turk. J. Earth Sci. 22, 747–777. https://doi.org/10.3906/yer-1207-10.

Okay, A.I., Topuz, G., 2017. Variscan orogeny in the Black Sea region. Int. J. Earth Sci. 106, 569–592. https://doi.org/10.1007/s00531-016-1395-z.

Ott, R.F., Gallen, S.F., Granger, D.E., 2022. Cosmogenic nuclide weathering biases: corrections and potential for denudation and weathering rate measurements. Geochronology 4, 455–470. https://doi.org/10.5194/gchron-4-455-2022.

Pavano, F., Gallen, S.F., 2021. A geomorphic examination of the Calabrian forearc translation. Tectonics 40, e2020TC006692. https://doi.org/10.1029/2020TC006692.

Perron, J.T., Royden, L., 2013. An integral approach to bedrock river profile analysis. Earth Surf. Process. Landf. 38, 570–576. https://doi.org/10.1002/esp.3302.

Racano, S., Schildgen, T.F., Cosentino, D., Miller, S.R., 2021. Temporal and spatial variations in rock uplift from river-profile inversions at the Central Anatolian Plateau southern margin. J. Geophys. Res., Earth Surf. 126, e2020JF006027. https://doi.org/10.1029/2020JF006027.

Reilinger, R., McClusky, S., Vernant, P., Lawrence, S., Ergintav, S., Cakmak, R., Ozener, H., Kadirov, F., Guliev, I., Stepanyan, R., Nadariya, M., Hahubia, G., Mahmoud, S., Sakr, K., ArRajehi, A., Paradissis, D., Al-Aydrus, A., Prilepin, M., Guseva, T., Evren, E., Dmitrotsa, A., Filikov, S.V., Gomez, F., Al-Ghazzi, R., Karam, G., 2006. GPS constraints on continental deformation in the Africa-Arabia-Eurasia continental collision zone and implications for the dynamics of plate interactions. J. Geophys. Res. 111. https://doi.org/10.1029/2005JB004051.

Riebe, C.S., Kirchner, J.W., Granger, D.E., 2021. Quantifying quart enrichment and its consequences for cosmogenic measurements of erosion rates from alluvial sediment and regolith. Geomorphology 40, 15–19. https://doi.org/10.1016/S0169-555X(01)00031-9.

Schildgen, T.F., Phillips, W.M., Purves, R.S., 2005. Simulation of snow shielding corrections for cosmogenic nuclide surface exposure studies. Geomorphology 64, 67–85. https://doi.org/10.1016/j.geomorph.2004.05.003.

Schwanghart, W., Scherler, D., 2014. Short communication: TopoToolbox 2 – MATLAB-based software for topographic analysis and modeling in Earth surface sciences. Earth Surf. Dyn. 2, 1–7. https://doi.org/10.5194/esurf-2-1-2014.

Şenel, M., 2002. Türkiye Jeoloji Haritası. In: Geological Map of Turkey (Sheets 19, Scale 1:500,000). Maden Tetk. ve Arama, Genel Müdürlüğü, Ankara.

Smith, A.G.G., Fox, M., Schwanghart, W., Carter, A., 2022. Comparing methods for calculating channel steepness index. Earth-Sci. Rev. 227, 103970. https://doi.org/10.1016/j.earscirev.2022.103970.

Şengör, A.M.C., Yilmaz, Y., 1981. Tethyan evolution of Turkey: a plate tectonic approach. Tectonophysics 75, 181–241. https://doi.org/10.1016/0040-1951(81)90275-4.

Şengör, A.M.C., Görür, N., Şaroğlu, F., 1985. Strike-slip faulting and related basin formation in zones of tectonic escape: Turkey as a case study. In: Biddle, K.T., Christie-Blick, C. (Eds.), Strike-Slip Deformation, Basin Formation and Sedimentation.

Şengör, A.M.C., Tüysüz, O., İmren, C., Sakınç, M., Eyidoğan, H., Görür, N., Le Pichon, X., Rangin, C., 2005. The North Anatolian Fault: a new look. Annu. Rev. Earth Planet. Sci. 33, 37–112. https://doi.org/10.1146/annurev.earth.32.101802.120415.

Sorlien, C.C., Akhun, S.D., Seeber, L., Steckler, M.S., Shillington, D.J., Kurt, H., Çifçi, G., Poyraz, D.T., Gürçay, S., Dondurur, D., İmren, C., Perinçek, E., Okay, S., Küçük, H.M., Diebold, J.B., 2012. Uniform basin growth over the last 500 ka, North Anatolian Fault, Marmara Sea, Turkey. Tectonophysics 518–521, 1–16. https://doi.org/10.1016/j.tecto.2011.10.006.

Ünay, E., Emre, Ö., Erkal, T., Keçer, M., 2001. The rodent fauna from the Adapazarıpull-apart basin (NW Anatolia): its bearings on the age of the North Anatolian fault. Geodin. Acta 14, 169–175. https://doi.org/10.1080/09853111.2001.11432442.

von Blanckenburg, F., Hewawasam, T., Kubik, P.W., 2004. Cosmogenic nuclide evidence for low weathering and denudation in the wet, tropical highlands of Sri Lanka. J. Geophys. Res., Earth Surf. 109. https://doi.org/10.1029/2003JF000049.

Whipple, K.X., Tucker, G.E., 1999. Dynamics of the stream-power river incision model: implications for height limits of mountain ranges, landscape response timescales, and research needs. J. Geophys. Res., Solid Earth 104, 17661–17674. https://doi.org/10.1029/1999JB900120.

Wittmann, H., von Blanckenburg, F., 2016. The geological significance of cosmogenic nuclides in large lowland river basins. Earth-Sci. Rev. 159, 118–141. https://doi.org/10.1016/j.earscirev.2016.06.001.

Wobus, C., Whipple, K.X., Kirby, E., Snyder, N., Johnson, J., Spyropolou, K., Crosby, B., Sheehan, D., 2006. Tectonics from topography: procedures, promise, and pitfalls. Geol. Soc. Am. Spec. Pap. 398, 55–74. https://doi.org/10.1130/2006.2398(04).

Yavaşoğlu, H., Tarı, E., Tüysüz, O., Çakı, r Z., Ergintav, S., 2011. Determining and modeling tectonic movements along the central part of the North Anatolian Fault (Turkey) using geodetic measurements. J. Geodyn. 51, 339–343. https://doi.org/10.1016/j.jog.2010.07.003.

Yildirim, C., Schildgen, T.F., Echtler, H., Melnick, D., Strecker, M.R., 2011. Late Neogene and active orogenic uplift in the Central Pontides associated with the North Anatolian Fault: implications for the northern margin of the Central Anatolian Plateau, Turkey. Tectonics 30. https://doi.org/10.1029/2010TC002756.

Yildirim, C., Schildgen, T.F., Echtler, H., Melnick, D., Bookhagen, B., Çiner, A., Niedermann, S., Merchel, S., Martschini, M., Steier, P., Strecker, M.R., 2013a. Tectonic implications of fluvial incision and pediment deformation at the northern margin of the Central Anatolian Plateau based on multiple cosmogenic nuclides. Tectonics 32, 1107–1120. https://doi.org/10.1002/tect.20066.

Yildirim, C., Melnick, D., Ballato, P., Schildgen, T.F., Echtler, H., Erginal, A.E., Kıyak, N.G., Strecker, M.R., 2013b. Differential uplift along the northern margin of the Central Anatolian Plateau: inferences from marine terraces. Quat. Sci. Rev. 81, 12–28. https://doi.org/10.1016/j.quascirev.2013.09.011.

Yıldırım, C., Tüysüz, O., 2017. Estimation of the long-term slip, surface uplift and block rotation along the northern strand of the North Anatolian Fault Zone: inferences from geomorphology of the Almacık Block. Geomorphology 297, 55–68. https://doi.org/10.1016/j.geomorph.2017.08.038.

Yolsal-Çevikbilen, S., Biryol, C.B., Beck, S., Zandt, G., Taymaz, T., Adiyaman, H.E., Özacar, A.A., 2012. 3-D crustal structure along the North Anatolian Fault Zone in north-central Anatolia revealed by local earthquake tomography. Geophys. J. Int. 188, 819–849. https://doi.org/10.1111/j.1365-246X.2011.05313.x.

XMLVIEW: extended

Appendix A. Supplementary material

The following is the Supplementary material related to this article.

begin ecomponent begin ecomponent begin ecomponent begin ecomponent begin ecomponent begin ecomponent begin ecomponent begin ecomponent begin ecomponent begin ecomponent begin ecomponent begin ecomponent begin ecomponent begin ecomponent begin ecomponent begin ecomponent begin ecomponent begin ecomponent

Label: MMC 1

caption: Appendix: Supplementary material The text in the supplementary material provides further details on the tectono-stratigraphic settings of the Central Pontides (1) and an extended description of the river linear inversion method applied in this work (2). Supplementary pictures show the calibration of the erodibility parameter (S1-S2), river linear inversion setup and calibration tests (S3-S14). Supplementary tables provide the percentage of area occupied by quartz-rich and quartz-poor rocks in the catchments used for river inversions (Tab. S1), and the average erodibility estimated for the main lithological classes (Tab. S2).

link: **APPLICATION : mmc1**

end ecomponent end ecomponent end ecomponent end ecomponent end ecomponent end ecomponent end ecomponent end ecomponent end ecomponent end ecomponent end ecomponent end ecomponent end ecomponent end ecomponent end ecomponent end ecomponent end ecomponent end ecomponent end ecomponent

begin ecomponent begin ecomponent begin ecomponent begin ecomponent begin ecomponent begin ecomponent begin ecomponent begin ecomponent begin ecomponent begin ecomponent begin ecomponent begin ecomponent begin ecomponent begin ecomponent begin ecomponent begin ecomponent begin ecomponent begin ecomponent

Label: MMC 2

caption: Percentage of area occupied by each lithology in the 19 catchments selected for river inversion.

link: **APPLICATION : mmc2**

end ecomponent end ecomponent end ecomponent end ecomponent end ecomponent end ecomponent end ecomponent end ecomponent end ecomponent end ecomponent end ecomponent end ecomponent end ecomponent end ecomponent end ecomponent end ecomponent end ecomponent end ecomponent end ecomponent

begin ecomponent begin ecomponent begin ecomponent begin ecomponent begin ecomponent begin ecomponent begin ecomponent begin ecomponent begin ecomponent begin ecomponent begin ecomponent begin ecomponent begin ecomponent begin ecomponent begin ecomponent begin ecomponent begin ecomponent begin ecomponent

Label: MMC 3

caption: k_{sn} and K median values $\pm 1\sigma$ of each lithology outcropping in the Sinop Range (values from violin plots in Fig. 2 and S13).

link: **APPLICATION : mmc3**

end ecomponent end ecomponent end ecomponent end ecomponent end ecomponent end ecomponent end ecomponent end ecomponent end ecomponent end ecomponent end ecomponent end ecomponent end ecomponent end ecomponent end ecomponent end ecomponent end ecomponent end ecomponent end ecomponent

Sponsor names

Do not correct this page. Please mark corrections to sponsor names and grant numbers in the main text.

Q18 **MIUR**, *country*=Italy, *grants*=

Highlights

- Rock-uplift history of Central Pontides from river linear inversions.
- The uplift event after 10 Ma dates the arrival of the North Anatolian Fault (NAF).
- The uplift migration provides the propagation rate of the NAF central segment.
- New insights about the propagation history of all the NAF segments.
- Linkage between NAF propagation rates and plate convergence directions.